



CHORUS

This is the accepted manuscript made available via CHORUS. The article has been published as:

Characterizing the impact of particle behavior at fracture intersections in three-dimensional discrete fracture networks

Thomas Sherman, Jeffrey D. Hyman, Diogo Bolster, Nataliia Makedonska, and Gowri Srinivasan

Phys. Rev. E **99**, 013110 — Published 25 January 2019

DOI: [10.1103/PhysRevE.99.013110](https://doi.org/10.1103/PhysRevE.99.013110)

Abstract

We characterize the influence of different intersection mixing rules for particle tracking simulations on transport properties through three-dimensional discrete fracture networks. It is too computationally burdensome to explicitly resolve all fluid dynamics within a large three-dimensional fracture network. In discrete fracture network (DFN) models, mass transport at fracture intersections is modeled as a sub-grid scale process based on a local Péclet number. The two most common mass transfer mixing rules are 1) complete mixing, where diffusion dominates mass transfer, and 2) streamline routing, where mass follows pathlines through an intersection. Although, it is accepted that mixing rules impact local mass transfer through single intersections, the effect of the mixing rule on transport at the fracture network scale is still unresolved. Through the use of explicit particle tracking simulations, we study transport through a quasi-two-dimensional lattice network and a three dimensional network whose fracture radii follow a truncated power law distribution. We find that the impact of the mixing rule is a function of the initial particle injection condition, the heterogeneity of the velocity field, and the geometry of the network. Furthermore, our particle tracking simulations show that the mixing rule can particularly impact concentrations on secondary flow pathways. We relate these local differences in concentration to reactive transport and show that streamline routing increases the average mixing rate in DFN simulations.

* Corresponding author: jhyman@lanl.gov

15 I. INTRODUCTION

16 The behavior of fluid flow and the associated transport of dissolved chemicals through
17 low-permeability subsurface rocks is primarily controlled by fracture networks within the
18 medium. Length scales within these networks typically range several orders of magni-
19 tude [1] and characterizing the interplay across these length scales has applications in a
20 range of engineering endeavors including CO₂ sequestration technologies [2], geothermal en-
21 ergy extraction [3], unconventional hydrocarbon extraction [4], and the long term storage
22 of spent nuclear fuel [5]. At the network structure scale, connectivity and density control
23 the general behavior of the fluid flow field [6]. Within individual fractures, the location of
24 inflow and outflow boundaries and local variations in the fracture aperture determine the
25 local flow field [7, 8]. However, how fluid moves through the intersections between fractures
26 is also important in terms of local dispersion because intersections are regions of enhanced
27 mixing [9] and can impact network scale spreading of solute [10].

28 Discrete fracture networks (DFN) are one of the most common modelling tools for sim-
29 ulating flow and transport through fractured media. In the DFN methodology fractures
30 are represented as lower dimensional structures in the domain, lines in two-dimensions and
31 planes in three-dimensions. The choice to explicitly resolve fractures, as opposed to using
32 effective properties in continuum models, allows observations of transport to be linked to
33 the structural properties of the fracture networks. This choice drastically increases the cost
34 of running DFN simulations and certain aspects of the simulation are modelled as sub-grid
35 scale processes.

36 One such subgrid process is particle behavior within fracture intersections. There have
37 been a number of laboratory experiments [9, 11–14] and numerical simulations [15–18] to
38 better understand particle behavior within fracture intersections. The fluid velocity field
39 along fracture intersections is three-dimensional and particle behavior is determined by the
40 combination of the velocity field, the velocity magnitude and diffusion. In a DFN, however,
41 the line of intersection is either a point (2D) or a line (3D) and the true structure of the
42 velocity field is not resolved. In attempts to represent the particle behavior several subgrid
43 processes have been proposed. The two most prominent fracture intersection rules are
44 complete mixing and streamline routing. Particle transport is primarily diffusion controlled
45 with the complete mixing rule and advection dominated with the streamline routing rule.

46 The choice of which process is most appropriate is determined by the local physics of the
47 fracture intersection, characterized by a Péclet number Pe , the ratio of advective to diffusive
48 forces. Assuming complete mixing can be traced to the fracture junction experiments of
49 Krizek et al. [11], where an inflowing branch intersected with multiple outflowing branches.
50 In these experiments, tracer from the inflow branch entered a junction and was distributed
51 to the multiple outflowing branches, which was interpreted as complete mixing of the tracer
52 within the junction. In a DFN model with a complete mixing subgrid process, particles enter
53 an intersection and are conceptually allowed to jump between streamlines and mix within
54 the intersection due to diffusion. In contrast, the streamline routing mixing rule prohibits
55 solute from crossing streamlines, implying only advection governs transport, representative
56 of a high Pe condition. Laboratory experimental observations of solute trajectories through
57 a single orthogonal intersection with two inflow and two outflow branches [12–14] suggest
58 streamline routing is appropriate when the intersection $Pe > O(10)$.

59 The aforementioned laboratory studies considered transport through an idealized intersec-
60 tion that is poorly representative of real geologic geometries. Moreover, they do not consider
61 the impact of particle behavior along intersections on transport at the fracture and network
62 scale. There have been several numerical simulations to address these aspects of DFN mod-
63 elling but their conclusions appear to be in disagreement. Park et al. [19] concluded that the
64 mixing rule did not significantly impact transport for simulations through two-dimensional
65 networks where fracture lengths were power law distributed and solute enters the domain via
66 a point source initial condition. Similarly, Cvetkovic et al. [5] simulated transport through
67 a three-dimensional DFN where particles were injected across an inlet plane, and concluded
68 that the mixing rule had little impact on transport as quantified by travel time distributions.
69 However, Kupper et al. [20], Park et al. [21], and Kang et al. [10] found that for a point
70 source initial condition complete mixing can enhance transverse spreading of a solute plume
71 compared to streamline routing for transport through certain two-dimensional lattice cases.
72 These studies suggest the impact of the mixing rule depends on the network structure, het-
73 erogeneity of the velocity field, dimensionality of the network, and initial injection mode of
74 particles. Thus, it is not clear under what conditions the choice of mixing rule at fracture
75 intersections has an impact on different large scale transport features.

76 We use DFNWORKS [22] to simulate transport through two different DFN structures
77 that represent varying degrees of structural and velocity field heterogeneity and study con-

78 ditions under which the mixing rule is important for transport through large scale fracture
79 networks. One network is a quasi-two-dimensional lattice where the apertures are sampled
80 from a lognormal distribution and the other is a set of networks composed of circular frac-
81 tures whose lengths are drawn from a power law distribution. In both sets of simulations,
82 we consider point injection and flux-weighted injection of particles across the entire inlet
83 plane. The impact of complete mixing and streamline routing is compared in terms of the
84 travel time distributions, mean squared displacement, and transverse breakthrough distribu-
85 tions of solute plumes at uniformly spaced control planes. Additionally, to explore possible
86 implications on mixing driven reactions we also compare mixing rates in simulations with
87 different implemented fracture intersection mixing rules.

88 We observe that the impact of the mixing rule depends on the initial injection mode,
89 the fracture network structure, and heterogeneity of the velocity field. The greatest impact
90 on upscaled properties is observed when particles are released from a point source. As
91 heterogeneity of the network structure increases particles tend to channelize at the network
92 scale and the impact of the mixing rule on upscaled behavior decreases. But even in highly
93 heterogenous systems, there are significant differences in transport behavior within fracture
94 planes where in-plane channelization is observed. Specifically, we find that streamline routing
95 increases channelization of mass to secondary fractures, resulting in an increased overall
96 system wide averaged mixing rate and local mixing rates that can differ by up to two
97 orders of magnitude. This has strong potential implications for reactive transport, mainly
98 in determining how aggressively and where mixing driven reactions will occur [23, 24].

99 II. DISCRETE FRACTURE NETWORK SIMULATIONS

100 There are a number of methods used to model flow and the associated transport of
101 dissolved chemical species through fractured media in the subsurface including stochastic
102 continuum [25], dual-porosity / dual-permeability [26], and discrete fracture network models
103 (DFN) [27–29]. Here we use the discrete fracture network (DFN) modeling methodology
104 where individual fractures are represented as planar $N - 1$ dimensional objects embedded
105 within an N dimensional space. Each fracture is assigned a shape, location, and orientation
106 within the domain by sampling distributions whose parameters reflect a site characteriza-
107 tion. The fractures form a network embedded within an impermeable rock matrix; we do not

108 consider interaction between flow within the fractures and the solid matrix. Each fracture is
 109 meshed for computation and the governing equations for flow and transport are numerically
 110 integrated on the network. The choice to use a DFN model rather than a continuum model
 111 arises due to the focus of this study, which is characterizing the influence of smaller scale
 112 processes, namely particle behavior at fracture intersections, on upscaled transport behav-
 113 ior. Continuum models do not explicitly represent fractures and their intersections and are
 114 therefore unsuitable for the task at hand.

115 The generation of each discrete fracture network along with flow and transport simu-
 116 lations is preformed using the DFNWORKS suite [22]. DFNWORKS is a high-fidelity DFN
 117 modelling suite that has been used in analysis of flow properties in fractured media with
 118 scales ranging from millimeters to kilometers and with applications in nuclear waster dis-
 119 posal [30, 31] and hydraulic fracturing [4, 32]. DFNWORKS combines the feature rejection
 120 algorithm(FRAM) [33], the LaGriT meshing toolbox [34], the parallelized subsurface flow
 121 and reactive transport code PFLOTRAN [26], and an extension of the WALKABOUT particle
 122 tracking method [35, 36]. FRAM is used to generate three-dimensional fracture networks.
 123 LaGriT is used to create a computational mesh representation of the DFN in parallel. PFLO-
 124 TRAN is used to numerically integrate the governing flow equations. WALKABOUT is used to
 125 determine pathlines through the DFN and simulate solute transport. Details of the suite,
 126 implementation, its abilities, applications, and references are provided in Hyman et al. [22].

127 A. Flow Simulations

128 Under the assumption of aperture uniformity within a single fracture, flow therein is
 129 equivalent to flow between two parallel plates and can be modeled with the Stokes equations,
 130 the governing equations for low Reynolds number isothermal single phase Newtonian flow.
 131 The Stokes equations can be integrated to determine the volumetric flow rate Q per unit
 132 fracture width normal to the direction of flow

$$\mathbf{Q} = \frac{-b^3}{12\mu} \nabla P, \quad (1)$$

133 i.e., the Boussinesq equation. Here b is the aperture height and P is pressure. We consider
 134 an incompressible fluid such that

$$\nabla \cdot \mathbf{Q} = 0 \quad . \quad (2)$$

135 Equation 1 and 2, along with boundary and initial conditions, are used to derive an elliptic
 136 partial differential equation for the steady-state distribution of pressure within a network

$$\nabla \cdot (b^3 \nabla P) = 0. \quad (3)$$

137 Once the distribution of pressure and volumetric flow rates are determined by numerically
 138 integrating (3), the Eulerian velocity field $\mathbf{u}(\mathbf{x})$ within the DFN is reconstructed from the
 139 volumetric fluxes and pressures following Makedonska et al. [35] and Painter et al. [36]. A
 140 pressure gradient is imposed, which is aligned with the x axis, making this also the primary
 141 direction of flow.

142 B. Transport Simulations: Particle Tracking

143 We represent the transport of a nonreactive conservative solute in the DFN using passive
 144 tracer particles, i.e., a Lagrangian approach. Particle motion is purely advective within a
 145 fracture and molecular diffusion is only considered in fracture intersections via a subgrid
 146 process. We denote the plume of particles as Ω and consider two different inlet conditions.
 147 The first inlet condition is a point source where all particles are released into a single fracture
 148 close to the center of the inlet plane. In the second inlet condition, particles are spread across
 149 the entire inlet plane and the number of particles at a given location is proportional to the
 150 flux entering the system at the location, i.e., a flux-weighted injection [30, 37, 38].

151 Each particle has a unique initial position that we denote $\mathbf{a} = (0, y, z)^\top$, where the
 152 superscript \top indicates the transpose. The trajectory $\mathbf{x}(t; \mathbf{a})$ of a particle starting at \mathbf{a} at
 153 time $t = 0$ is given by the advection equation

$$\frac{d\mathbf{x}(t; \mathbf{a})}{dt} = \mathbf{v}_t(t; \mathbf{a}), \quad \mathbf{x}(0; \mathbf{a}) = \mathbf{a}, \quad (4)$$

154 where the Lagrangian velocity $\mathbf{v}_t(t; \mathbf{a})$ is given in terms of the Eulerian velocity $\mathbf{u}(\mathbf{x})$ as

$$\mathbf{v}_t(t; \mathbf{a}) = \mathbf{u}[\mathbf{x}(t; \mathbf{a})]. \quad (5)$$

155 The length $\ell(t; \mathbf{a})$ of the trajectory at a time t is

$$\frac{d\ell(t; \mathbf{a})}{dt} = v_t(t, \mathbf{a}). \quad (6)$$

156 where the Lagrangian velocity is the velocity magnitude $v_t(t, \mathbf{a}) = |\mathbf{v}_t(t, \mathbf{a})|$. The length of
 157 the pathline, ℓ , is used to parameterize the spatial and temporal coordinates of the particle.

158 Within the domain, we consider uniformly spaced control planes that are perpendicular
 159 to the primary direction of flow. The first arrival time $\tau(x_i; \mathbf{a})$ of a particle at a control
 160 plane located at x_i from the inlet is given by

$$\tau(x_i; \mathbf{a}) = t[\lambda(x_i); \mathbf{a}], \quad \lambda(x_i) = \inf\{\ell | x_i(\ell; \mathbf{a}) \geq x_i\}. \quad (7)$$

161 C. Measurements

162 At every control plane x_i , the first arrival times of the particles (Eq. 7) are combined to
 163 obtain the cumulative distribution of travel times for the plume of particles

$$\psi(t, x_i) = \frac{1}{M} \int d\Omega H(t - \tau(x_i, \mathbf{a})) \quad (8)$$

164 Here, M is the total mass of all the particles $M = \int d\Omega$ and $H(t)$ is the heavy side function.
 165 We refer to $\psi(t, x)$ as the breakthrough curve. We also compute the transverse spreading
 166 using the distribution of particle positions at each control plane. Denoting the position of
 167 each particle at the control plane x_i as \mathbf{z}_x the transverse breakthrough position distribution
 168 (TBPD) in z is

$$f_{x_i}(z_k) = \frac{1}{M} \int d\Omega \delta(z_k - \mathbf{z}_{x_i}), \quad (9)$$

169 where δ is the Dirac delta function. An analogous equation is used to calculate TBPD in y .

170 The characteristic spreading of the particle plume in the transverse direction at longitu-
 171 dinal position x is quantified by the mean squared displacement,

$$MSD_x = \frac{1}{M} \int d\Omega (\bar{\mathbf{z}}_x - \mathbf{z}_x)^2 + (\bar{\mathbf{y}}_x - \mathbf{y}_x)^2, \quad (10)$$

172 where $\mathbf{z}_x, \mathbf{y}_x$ are vectors of the transverse position for each particle at x and the overline
 173 denotes the average over all particles.

174 III. PARTICLE BEHAVIOR AT FRACTURE INTERSECTIONS

175 When a particle arrives at a fracture intersection, both advective and diffusive processes
 176 should govern motion through the intersection. In a purely advective system, particle motion
 177 follows the streamlines of the velocity field. However, diffusion enables particles to jump
 178 between streamlines and mix. The amount of mixing that occurs in a fracture intersection

179 is a balance of the strength of advection relative to diffusion which can be characterized by
180 Péclet number

$$Pe = \frac{vL}{2D_m}. \quad (11)$$

181 We adopt the Pe definition provided in [15] where v is the average velocity within the
182 intersection, L is a characteristic diagonal distance across the intersection, and D_m is the
183 molecular diffusion coefficient.

184 The upscaled nature of DFN models prevents the detailed physics that control mass
185 transfer at fracture intersections from being resolved. Instead, subgrid processes are used to
186 model mass transfer through intersections. There are two mixing rules that are commonly
187 applied: 1) complete mixing and 2) streamline routing. These rules are representative of
188 end members associated with diffusion and advective controlled transport, respectively. The
189 choice of which rule to apply should reflect the physics of the intersection, as determined by
190 the Pe .

191 At a fracture intersection, conservation of mass requires that the sum of incoming and
192 outgoing Darcy fluxes is zero, $\sum_i q_i = 0$. Both mixing rules require knowledge of the Darcy
193 outflowing fluxes. The streamline routing rule needs additional information, the position
194 of the inflow branches relative to each outflow branch and so implementation of complete
195 mixing at fracture intersections is simpler than streamline routing.

196 1. Complete Mixing

197 Under complete mixing, particle motion within the intersection is controlled by diffusion.
198 In this scenario, particles enter an intersection inlet and are conceptually allowed to jump
199 between streamlines by being re-positioned to any point within the intersection with equal
200 probability. Figure 1 (a) shows mass transfer under the complete mixing rule in a single
201 orthogonal intersection where all branches have an equivalent discharge magnitude. Light
202 blue mass from the top inlet and red mass from the bottom inlet mix at the intersection
203 and are distributed equally between the two outflowing branches. Each outlet contains mass
204 from both inlets, represented by the outflowing purple color in the figure.

205 With complete mixing the probability a particle exits a given outlet is proportional to
206 the outlet flux, mathematically represented as,

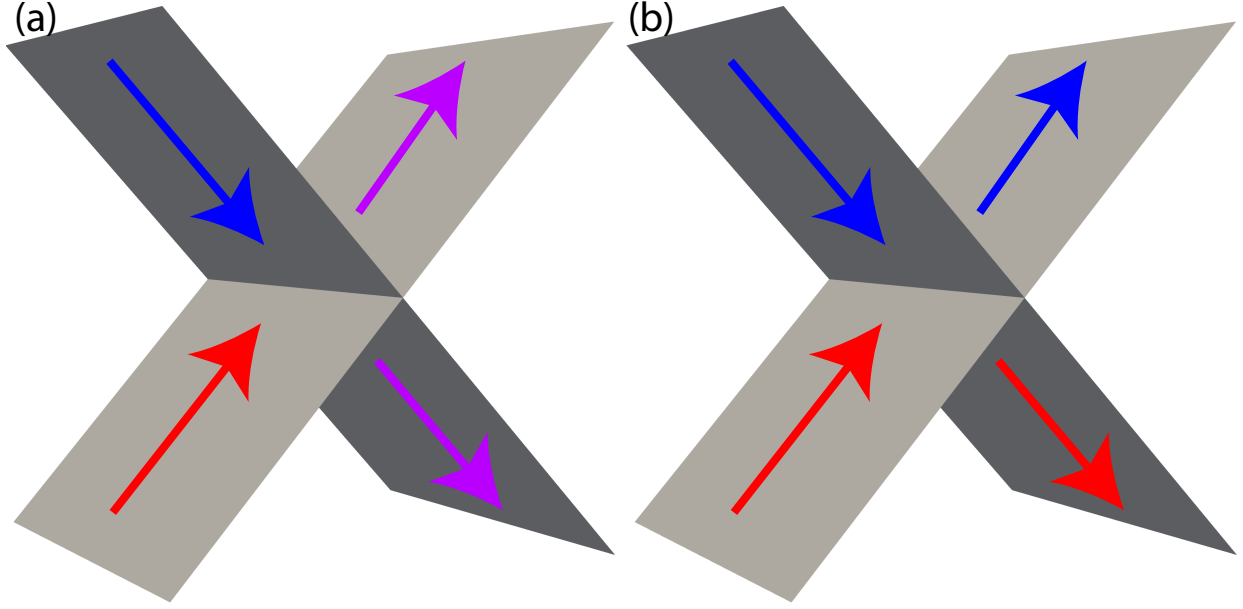


FIG. 1. A fracture intersection with two inflow branches and two outflow branches. All branches have equivalent discharge magnitudes. In complete mixing (a) mass from both inlets (red and blue) mix at the intersection and mass is distributed equally to each outlet (purple). In streamline routing (b) incoming red mass from the bottom inlet and blue mass from the top inlet are forced to their respective adjacent fractures and do not mix.

$$p_j = \frac{|q_j|}{\sum_k |q_k|}, \quad (12)$$

where p_j is the probability a particle exits outlet j , and k denotes an outflowing fracture branch.

2. Streamline Routing

In the streamline routing rule particle motion through fracture intersections is advection controlled. Particles adhere to their respective streamlines through the intersection, as if no mixing occurs within the intersection. Therefore, particle motion depends on the particle's inlet position. The streamline routing rule differs from the complete mixing rule only when a fracture intersection has multiple incoming and multiple outflowing branches. In a two fracture intersection there are only two intersection types that have this geometry a) continuous junctions and b) discontinuous junctions [13].

217 A continuous junction has two inflowing branches, two outflowing branches, and the
 218 inflowing branches are adjacent, i.e. lie on different fractures. Figure 1 (b) depicts streamline
 219 routing mass transfer through a continuous junction where all branches have equivalent
 220 discharge magnitudes. Flow from an inlet is directed to the outflowing adjacent branch. In
 221 this case, all mass from each inlet is distributed to the adjacent outflowing branch because
 222 there is no mixing within the fracture intersection. In general, the streamline routing rule
 223 goes as follows. If discharge from the inlet is less than the adjacent outlet discharge, all
 224 mass is directed to the adjacent outlet. If the inlet discharge exceeds the adjacent outlet
 225 discharge, conservation of mass requires that the adjacent outlet is filled and excess mass is
 226 directed to the other outlet.

227 Consider a particle entering a continuous junction from an inlet with flux q_{in} , which is
 228 adjacent to an outflow branch with flux q_{adj} . The second (opposite) outflow branch lies
 229 on the same fracture as the initial inlet fracture and has flux q_{opp} . The streamline routing
 230 rule dictates that the probabilities of transitioning from the inlet to the adjacent p_{adj} and
 231 opposite p_{opp} outflow branches are:

$$p_{adj} = \begin{cases} 1, & q_{adj} \geq q_{in} \\ \frac{q_{adj}}{q_{in}}, & q_{adj} < q_{in} \end{cases}, \quad p_{opp} = 1 - p_{adj} \quad (13)$$

232 More details on continuous junctions are found in Hull et al. [13].

233 Discontinuous junctions arise from multiple sources and sinks present in the fracture
 234 network, such as a geothermal field with production and injection wells [13]. In a discon-
 235 tinuous junction inflowing branches are opposite and lay on the same fracture. Hull et al.
 236 [13] proposed two distributions of streamline routing through a four branch discontinuous
 237 intersection, one equivalent to complete mixing and one where the high discharge inlet is
 238 preferentially directed to the high discharge outlet. Philip [39] extended Hull's analysis by
 239 finding solutions for Laplace and Stokes flow through the orthogonal intersections. Philip
 240 showed that under certain conditions, mainly when there is significant differences in branch
 241 discharge magnitudes, using complete mixing for streamline routing can result in significant
 242 error. However, Hull's other proposed streamline routing rule, where the high discharge
 243 inlet is preferentially directed to the high discharge outlet, is also prone to error as adja-
 244 cent streamlines can have opposite directions for a considerable distance. Hence, the theory
 245 for streamline routing through discontinuous intersections is still not fully developed. For

246 completeness, we present Hull’s second proposed streamline routing rule for discontinuous
 247 intersections. In this case, mass from the higher discharge incoming branch q_{in}^{max} is parti-
 248 tioned to the higher discharge outflowing branch q_{out}^{max} and any excess mass exits the smaller
 249 discharge outflowing branch q_{out}^{min} . A particle arriving from the inlet with q_{in}^{max} has outlet
 250 transition probabilities given by

$$p_{out}^{max} = \begin{cases} 1, & q_{out}^{max} \geq q_{in}^{max} \\ \frac{q_{out}^{max}}{q_{in}^{max}}, & q_{out}^{max} < q_{in}^{max} \end{cases}, \quad p_{out}^{min} = 1 - p_{out}^{max} \quad (14)$$

251 A particle arriving from the weaker inflow branch has transition probabilities:

$$p_{out}^{max} = \begin{cases} \frac{q_{out}^{max} - q_{in}^{min}}{q_{in}^{min}}, & q_{out}^{max} \geq q_{in}^{min} \\ 0, & q_{out}^{max} < q_{in}^{min} \end{cases}, \quad p_{out}^{min} = 1 - p_{out}^{max} \quad (15)$$

252 We performed simulations using both of Hull’s discontinuous streamline routing rules. Re-
 253 sults were not effected by different rules due in part to the observation that discontinuous
 254 intersections are rare in the systems under consideration. Our presented results are only
 255 shown for the case described above.

256 The occurrence and frequency of triple intersections, where three fractures come together
 257 at point, depends on the particular fractured media under consideration. However, these
 258 triple intersections do occur regularly in unconstrained stochastically generated DFN, their
 259 frequency depends on the fracture length distribution, network density, and fracture family
 260 orientation. Thus, from a practical and computational point of view, a rule for particle
 261 behavior at these points needs to be adopted in DFN modeling. We apply complete mixing
 262 at all triple intersections primarily due to the lack of experimental data concerning flow
 263 properties at triple intersections by which to verify appropriate streamline routing rules.

264 IV. RESULTS

265 A. Sample Fracture Networks

266 We consider flow and transport within two distinct fracture network structures. The first
 267 is a quasi-two-dimensional lattice network and the second is a set of stochastically generated
 268 networks, where fracture radii are sampled from a truncated power law distribution. These

269 two network structures are considered because they display different features that drive
270 flow channelization. The lattice networks have an idealized, regular geometry and flow
271 channelization arises from variations in the permeability field. In the truncated power law
272 networks, fracture intersections are less frequent and the geometry of the network drives
273 flow channelization. In the analysis of results we non-dimensionalize distance with l^* , the
274 maximum fracture radius in the system, and time with τ^* , the time required to traverse l^*
275 traveling at the mean particle velocity.

276 1. *Lattice Network*

277 The lattice network is comprised of two sets of 50 parallel 3-dimensional planar fractures,
278 where fractures in each set are spaced one meter apart and intersect fractures of the other
279 sets at a 45° angle. The computational domain has size $[32, 1, 16]$ m in the x, y, z directions.
280 A pressure gradient of 1 MPa is used to drive flow in the x-direction. The imposed pressure
281 field results in a quasi-two-dimensional velocity field because velocity in y is negligible.

282 Fracture apertures are sampled from a lognormal distribution in accordance with obser-
283 vations [40–42]. Each lattice network has a mean aperture $\bar{b} = 10^{-4}$ m and three aperture
284 variance cases are considered, $\sigma_{\ln(b)}^2 = 0.1, 0.5, 1$. Twenty-five realizations are generated
285 for each mixing rule and aperture variance combination. For each combination, transport
286 is simulated for both point source and flux weighted initial injections. These simulations
287 are similar to the 2D lattice simulations of Kang et. al [10]. However, in our experiments
288 velocity field heterogeneity is controlled by changing the distribution of aperture sizes and
289 we consider an additional flux weighted initial injection case. The objective of studying
290 this network set is to fix the network structure and focus on the effects of variability at the
291 fracture scale.

292 2. *Truncated Power-law Network*

293 The second set of networks are composed of disk-shaped fractures whose radii are sampled
294 from a truncated power-law distribution, which is a commonly observed length distribution
295 in field data [1, 43–45]. Bour and Davy [43] showed a power-law distribution accurately
296 captures the wide range of fracture lengths often observed in geological datasets [44, 45]. In

297 our power law networks, fracture radii are sampled from a truncated power-law distribution
 298 with exponent α and upper and lower cut-offs of $(R_u; R_0)$

$$R = R_0 \left[1 - \eta + \eta \left(\frac{R_0}{R_u} \right)^\alpha \right]^{-1/\alpha}, \quad (16)$$

299 where η is a random number sampled from a uniform distribution on $[0,1]$. We choose an
 300 exponent $\alpha = 2.1$ and cut-offs $R_0 = 2 R_u = 30\text{m}$ based on field data [1, 46]. The networks are
 301 not meant to be realizations of the networks reported in [1] and [46], but rather semi-generic
 302 fracture networks. Fracture orientations are uniformly random and centers are uniformly
 303 distributed throughout the domain. Fracture apertures are positively correlated to their
 304 radius, $b = 5 \cdot 10^{-5} \cdot \sqrt{R}$, which controls the hydraulic properties within the fracture. This
 305 correlation between fracture size and aperture is common in DFN models [29, 31, 47–50]. The
 306 computational domain is a cube with sides of length 100m. We refer to these as truncated
 307 power law (TPL) networks.

308 Ten independent identically distributed network realizations are generated. We stop the
 309 generation of the networks once 1000 fractures are accepted into the network. This results in
 310 a network that is about 7 times more denser a network at the percolation threshold defined
 311 by [7, 51]. This procedure ensures that there is a subnetwork that connects inflow to outflow
 312 boundaries. To reduce computational cost, we remove all isolated clusters of fractures, those
 313 that do not connect inflow to outflow boundaries, because they do not contribute to
 314 flow. There are roughly 200 fractures the final networks and the average fracture intensity
 315 (P_{32} : Surface area over total volume) is approximately 0.1. Flow is forced along the x -axis by
 316 imposing constant pressure conditions at the inlet and outlet control planes perpendicular
 317 to x . The pressure difference in x across the inflow and outflow boundary is 1MPa.

318 B. Lattice Network Simulations

319 1. Breakthrough Curves: Lattice

320 Figure 3 shows the cumulative distribution of first passage arrival times (Eq. 8) for the
 321 point injection (a) and flux weighted (b) initial conditions. Thick lines (streamline routing)
 322 and stars (complete mixing) are median breakthrough curves for twenty-five realizations and
 323 transparent lines correspond to single realizations. For each realization, solid lines indicate

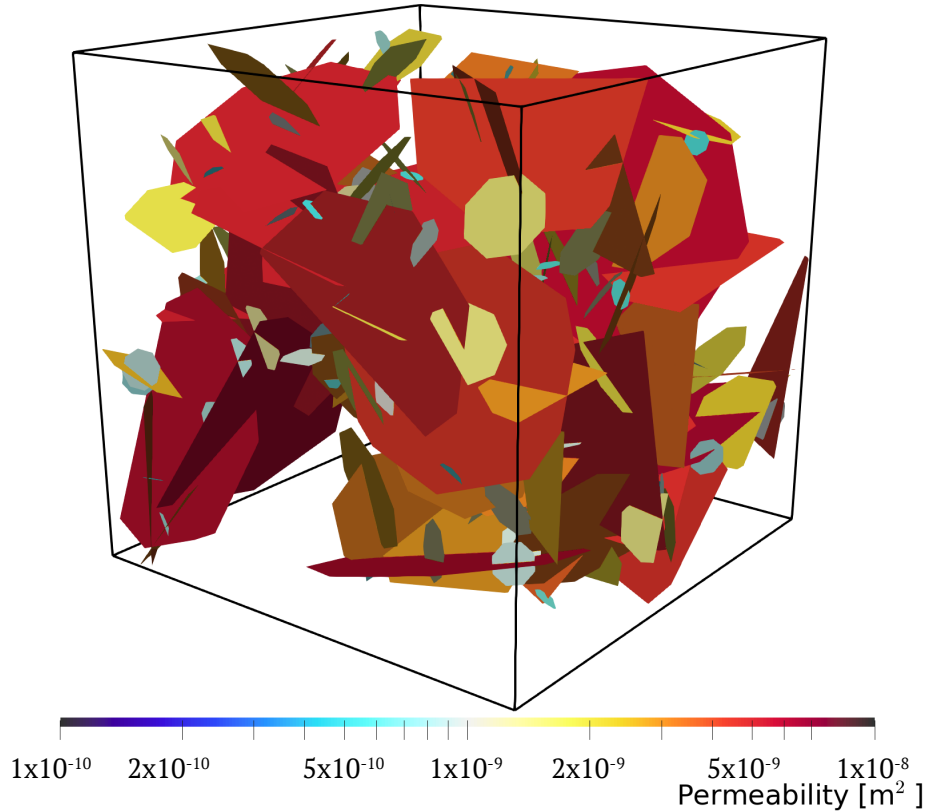


FIG. 2. One realization of a DFN with fracture lengths drawn from a power law distribution. Fractures are colored by their permeability, which is positively correlated with fracture radius.

324 streamline routing and dashed lines indicate complete mixing. Colors correspond to different
 325 aperture variances; $\sigma_{ln(b)}^2 = 0.1, 0.5, 1$ are depicted with blue, red, and green, respectively.
 326 As velocity field heterogeneity decreases, breakthrough curve realizations homogenize and
 327 the range of arrival times decreases. In both injection conditions and for all values of $\sigma_{ln(b)}^2$
 328 there is little impact of the mixing rule on the median observed travel time distributions.
 329 In turn, these results indicate that the mixing rule has no major impact on mean particle
 330 velocities, demonstrated by no significant change in breakthrough curve behavior (Figure
 331 3). Additionally, breakthrough curve realizations are more clustered near the median break-
 332 through curve for the flux weighted initial condition, e.g. the range of P_{50} values, the time
 333 at which 50% of mass has crossed the outlet control plane, decreases with the flux weighted
 334 case.

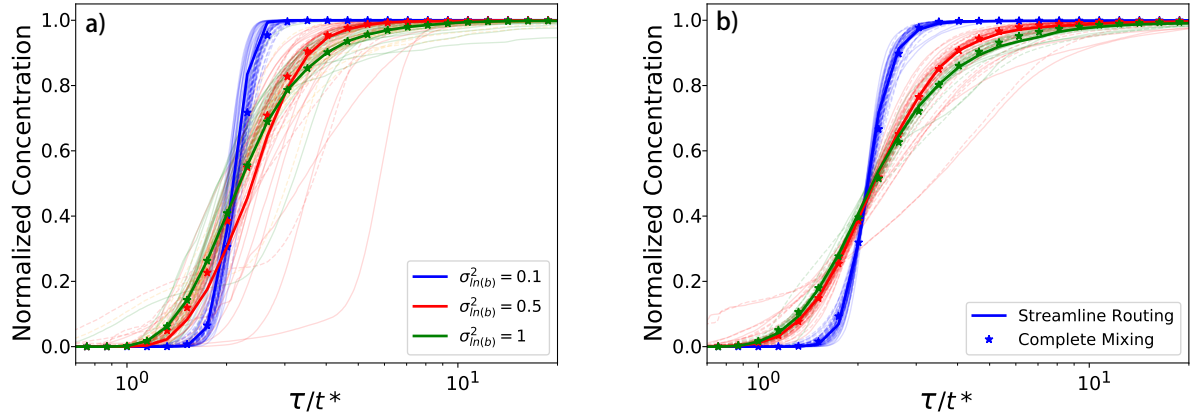


FIG. 3. Cumulative distribution of first passage arrival times (breakthrough curves) for point injection (a) and flux weighted (b) initial condition. Thick lines are median breakthrough curves for 25 realizations and transparent lines correspond to single realizations. For each realization, a solid lines indicate streamline routing and dashed lines indicate complete mixing. Colors correspond to different aperture variances; $\sigma_{ln(b)}^2 = 0.1, 0.5, 1$ are depicted with blue (steepest slope), red, and green (least steep slope), respectively.

335 2. Solute Spreading: Lattice

336 Figure 4 shows the spatial evolution of the transverse breakthrough position distribution
 337 $f_{x_i}(z)$ for simulated flow and transport through single realizations of lattice networks of
 338 varying velocity field heterogeneities with a point source injection initial condition. The
 339 top row shows $f_{x_i}(z)$ for complete mixing, the middle is for streamline routing and the
 340 bottom shows the ratio of streamline routing to complete mixing transverse breakthrough
 341 position concentrations. In each column, the streamline routing and complete mixing lattice
 342 networks are identical realizations. Colors are the logarithm of the concentration with yellow
 343 corresponding to relatively high concentration values and blue corresponding to lower values.
 344 In both mixing rule cases, there is more pronounced flow channeling as $\sigma_{ln(b)}^2$ increases due to
 345 the formation of paths of lower resistance. We calculate the percent of particles concentrated
 346 on each fracture at each control plane. As heterogeneity increases from $\sigma_{ln(b)}^2 = 0.1$ to
 347 $\sigma_{ln(b)}^2 = 1$, the largest value of percent particles on a single fracture increases by nearly a
 348 factor of 2 at distances greater than $x/l^* > 1$, demonstrating increased flow channelization
 349 (results not shown).

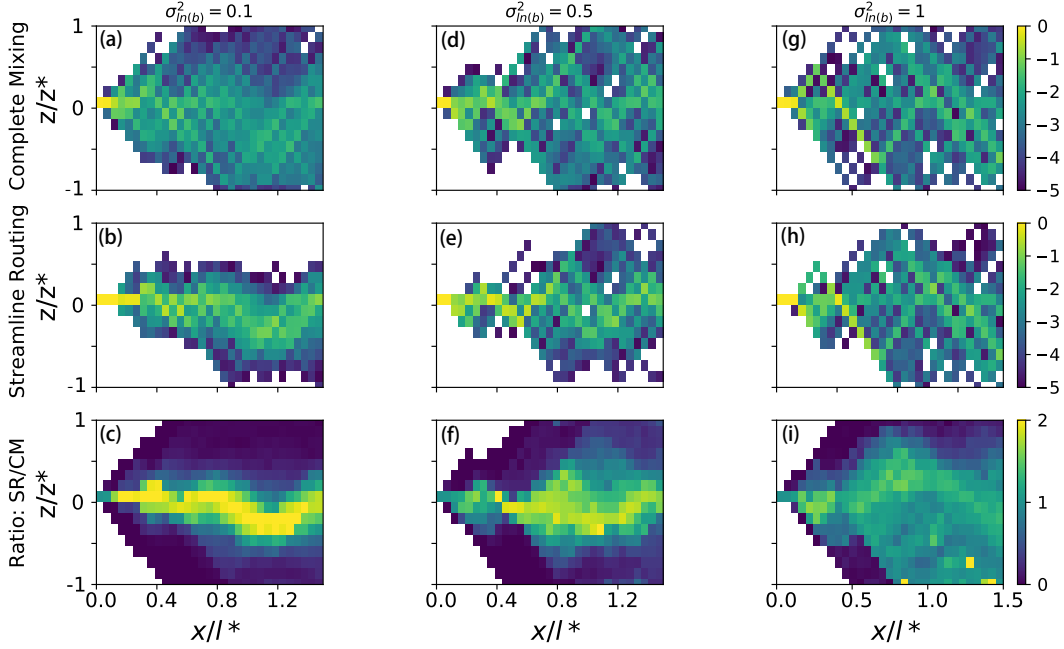


FIG. 4. The transverse distribution at sequential control planes through a lattice network with a point injection initial condition for one realization. All lattices have the same mean aperture size. Variance of aperture size is selected from a lognormal distribution and increases from the left to right column. Simulations are completed for complete mixing (row 1) and streamline routing (row 2) intersection rules for the same network realization. Row 3 gives the ratio of streamline routing to complete mixing transverse breakthrough position concentrations. Colorbars show log probabilities (rows 1,2) and absolute ratio values (row 3). Complete mixing enhances particle spreading. As velocity field heterogeneity increases, the impact of the mixing rule on particle spreading decreases. The transverse direction z is normalized by half the length the of domain z^* .

350 When complete mixing is used, the particles disperse transversely faster than in this case
351 of streamline routing and the plume reaches the lateral boundary of the domain closer to the
352 inlet. By contrast, streamline routing increases channelization, which is most notable at low
353 values of $\sigma_{ln(b)}^2$. Hence, both streamline routing and increasing velocity field heterogeneity
354 increase channelization of particles. The ratio of the streamline to complete mixing TBPD
355 highlights how the evolution of $f_{x_i}(z)$ changes because of the intersection mixing rule. Areas
356 of dark blue have value 0, indicating positions where breakthrough occurred under complete
357 mixing but not streamline routing. The yellow areas through the center of the lattice show

358 fractures where streamline routing increases particle concentration.

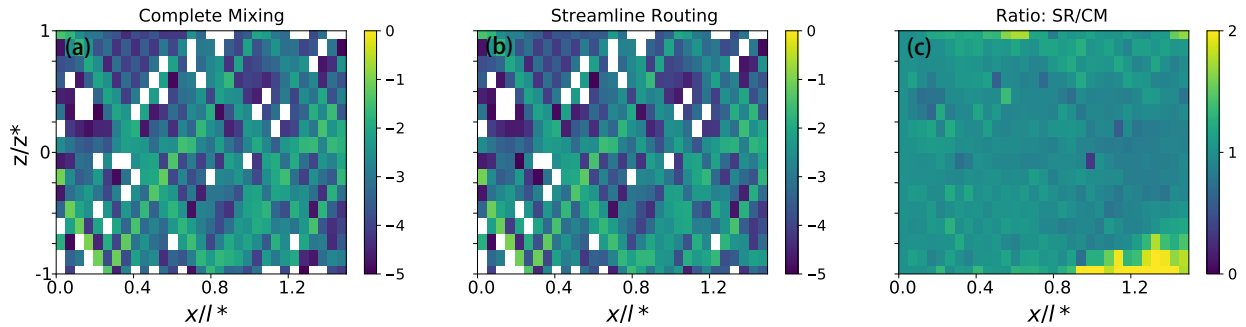


FIG. 5. The transverse breakthrough position distribution at each control plane for one realization of the lattice with a flux weighted injection. Simulations are completed for complete mixing (a) and streamline routing (b) intersection rules. Subfigure c gives the ratio of streamline routing to complete mixing transverse breakthrough position concentrations. Colorbars show log probabilities (row a,b) and the absolute ratio (c). $\sigma_{ln(b)}^2 = 0.5$ is the only aperture variance shown because results do not significantly change for different velocity field heterogeneities. The mixing rule has less impact on particle spreading with a flux weighted initial condition. The transverse direction z is normalized by half the length the of domain z^* .

359 Figure 5 shows the same plots as in Fig. 4 for a flux weighted injection. Only the $\sigma_b^2 = 0.5$
 360 is provided as all σ_b^2 values displayed nearly identical behavior. The ratio of streamline
 361 routing to complete mixing for $f_{x_i}(z)$ is close to 1 throughout much of the domain, indicating
 362 nearly identical distribution of the solute plume for the two mixing rules. One exception is
 363 the area of yellow in the bottom right corner of the ratio figure (c), where streamline routing
 364 has a higher particle concentration. This is an area of low particle concentrations and is
 365 therefore more sensitive. The results presented here indicate that the mixing rule's impact
 366 on the evolution of $f_{x_i}(z)$ is less significant when particles are injected using a flux weighted
 367 initial condition.

368 To demonstrate these differences, Figure 6 shows particles within one realization of the
 369 lattice network with $\sigma_{ln(b)}^2 = 1.0$ where fractures are colored by pressure. The left sub-figure
 370 (a) is a snapshot of particles injected from a point injection where the complete mixing rule
 371 is applied and in the middle sub-figure (b) streamline routing is applied. As discussed above,
 372 the application of the complete mixing rule leads to higher transverse dispersion when com-

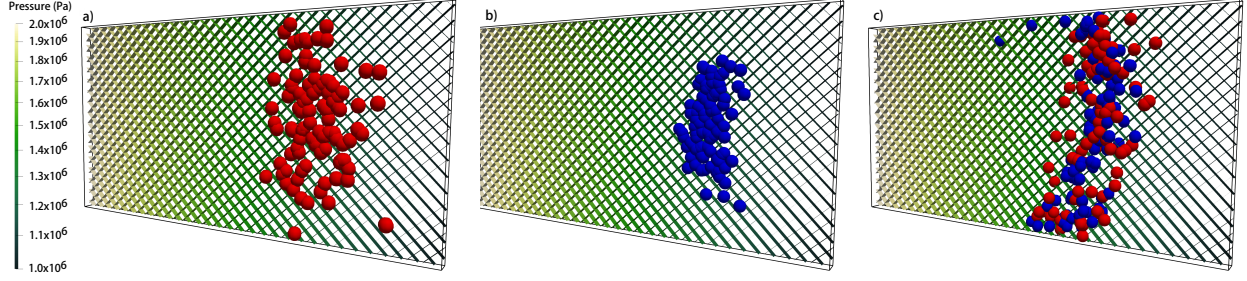


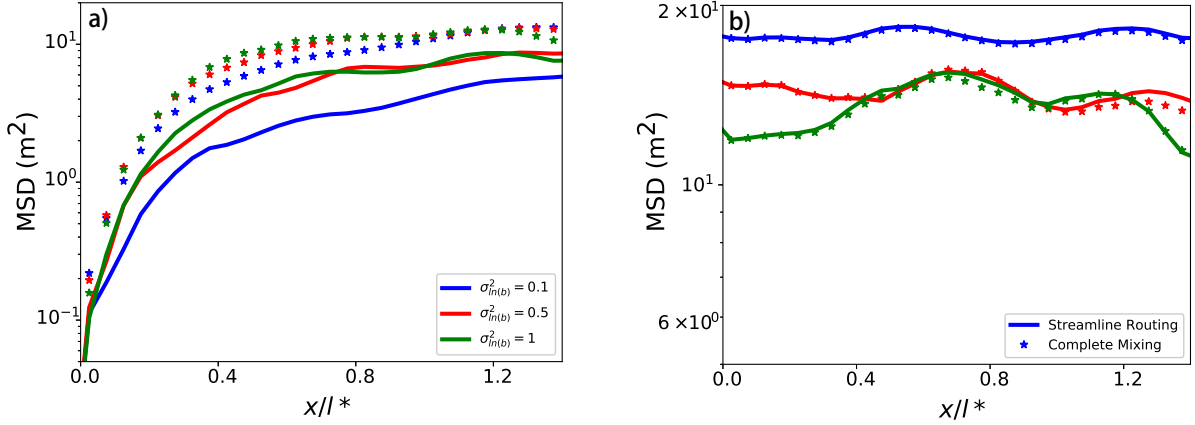
FIG. 6. Particles within the quasi-two-dimensional lattice network. In the left (a) and middle (b) sub-figures particles injected from the same point source on the left boundary and driven right by a pressure gradient. In sub-figure (a), particles adhere to a complete mixing rule (red) and in sub-figure (b) they follow streamline routing (blue). The choice of a complete mixing rule in combination with a point injection leads to higher transverse dispersion than if streamline routing is used under the same initial conditions. Sub-figure (c) shows particles injected using flux-weighting adhering to both mixing rules (red-complete mixing / blue-streamline routing). Here, no significant difference between the distribution of particle locations between the two rules is observed.

pared to streamline routing. The right sub-figure (c) shows both particles (red-complete
 373 mixing / blue-streamline routing) injected using flux-weighting. Here, no significant differ-
 374 ence between the distribution of particle locations between the two rules is observed.
 375

Figure 7 shows the mean value of the mean squared displacement (MSD) for point (a)
 376 and flux-weighted (b) initial conditions. These are calculated at each control plane by
 377 averaging over all particles and all 25 realizations. Solid lines indicate streamline routing and
 378 stars indicate complete mixing. Colors correspond to different aperture variances; $\sigma_{ln(b)}^2 =$
 379 0.1, 0.5, 1 are depicted with blue, red, and green, respectively.
 380

For the point injection, there is a significant difference between the observed MSD values
 381 for complete mixing and streamline routing. For all values of $\sigma_{ln(b)}^2$ complete mixing results
 382 in an increased MSD. The impact of the mixing rule on MSD decreases with increasing
 383 velocity field heterogeneity, shown by a decreasing difference in MSD between mixing rules.
 384 For the flux weighted injection the mixing rule's impact on MSD is less than in the point
 385 injection case, as the complete mixing and streamline routing curves more closely match.
 386 Note that the MSD is driven by displacements in the z direction due to the quasi-2D nature
 387 of the lattice.
 388

In the point injection, the number of times particles change fractures averaged over all
 389



55

FIG. 7. The mean MSD in the lattice network is calculated at each control plane by averaging over all particles and all 25 realizations. Solid lines indicate streamline routing and stars indicate complete mixing. Plotted is MSD for both the point (a) and flux weighted (b) initial conditions. Colors correspond to different aperture variances; $\sigma_{ln(b)}^2 = 0.1, 0.5, 1$ are depicted with blue (upper curve in b), red, and green (lower curve in b), respectively. As velocity field heterogeneity increases the mixing rule's impact on MSD decreases. A flux weighted injection results in less spatial variability of MSD.

390 particles and over 25 realizations increases for streamline routing by 52, 36 and 33% for
 391 $\sigma_{ln(b)}^2 = 0.1, 0.5, 1$, respectively. As the velocity field heterogeneity increases, particles change
 392 fractures less frequently due to increased channelization to high discharge pathways. In the
 393 case of flux-weighted injection, streamline routing increases the mean number of times a
 394 particle changes fractures by 52, 39, and 36% for $\sigma_{ln(b)}^2 = 0.1, 0.5, 1$ compared with complete
 395 mixing. Again as the velocity field heterogeneity increases particles change fractures less
 396 often and more particles are channelized to high discharge fractures.

397 C. Power Law Networks Simulations

398 1. Breakthrough Curves: TPL Network

399 The median breakthrough curves through the ten truncated power law (TPL) realizations
 400 for complete mixing (green stars) and streamline routing (thick orange lines) are shown in
 401 Figure 8. Solid lines correspond to point injections and dashed lines correspond to a flux

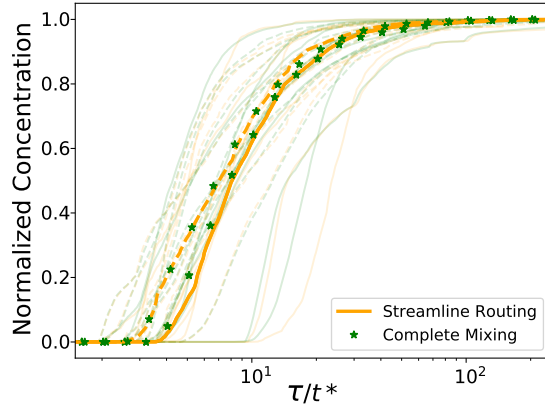


FIG. 8. Median breakthrough curves of 10 TPL realizations for complete mixing (green stars) and streamline routing (thick orange lines). Solid lines correspond to point injections and dashed lines correspond to a flux weighted initial condition. Each breakthrough curve realization is plotted with a transparent line. The mixing rule has a negligible impact of the distribution of arrival times. A flux weighted initial conditions homogenizes the spread of breakthrough curves.

402 weighted initial condition. Each breakthrough curve realization is plotted with a transparent
 403 line. No significant difference in the breakthrough curves is observed between the two mixing
 404 rules indicating that the choice of mixing rule has a negligible impact of the distribution of
 405 arrival times. The breakthrough curve is changed in two ways when using the flux weighted
 406 injection. First, breakthrough curves are shifted left, meaning particles on average traverse
 407 the entire network in less time compared with a point injection. This indicates that on
 408 average, the selected flow paths resulting from the sampled point injection in this study are
 409 slower than the flux weighted velocity average. However, given a larger sample of networks,
 410 we expect median breakthrough curves to converge. Second, the variability in breakthrough
 411 arrival times decreases with the flux weighted injection; the flux weighted breakthrough
 412 curves are more clustered near the median, whereas the point injection breakthrough curves
 413 display greater variation in arrival time for an associated cumulative concentration value.

414 2. Solute Spreading: TPL Network

415 Figure 9 shows the transverse breakthrough position distributions in z for one realization
 416 of a truncated power law distributed radii network for the point (a) and flux weighted (b)

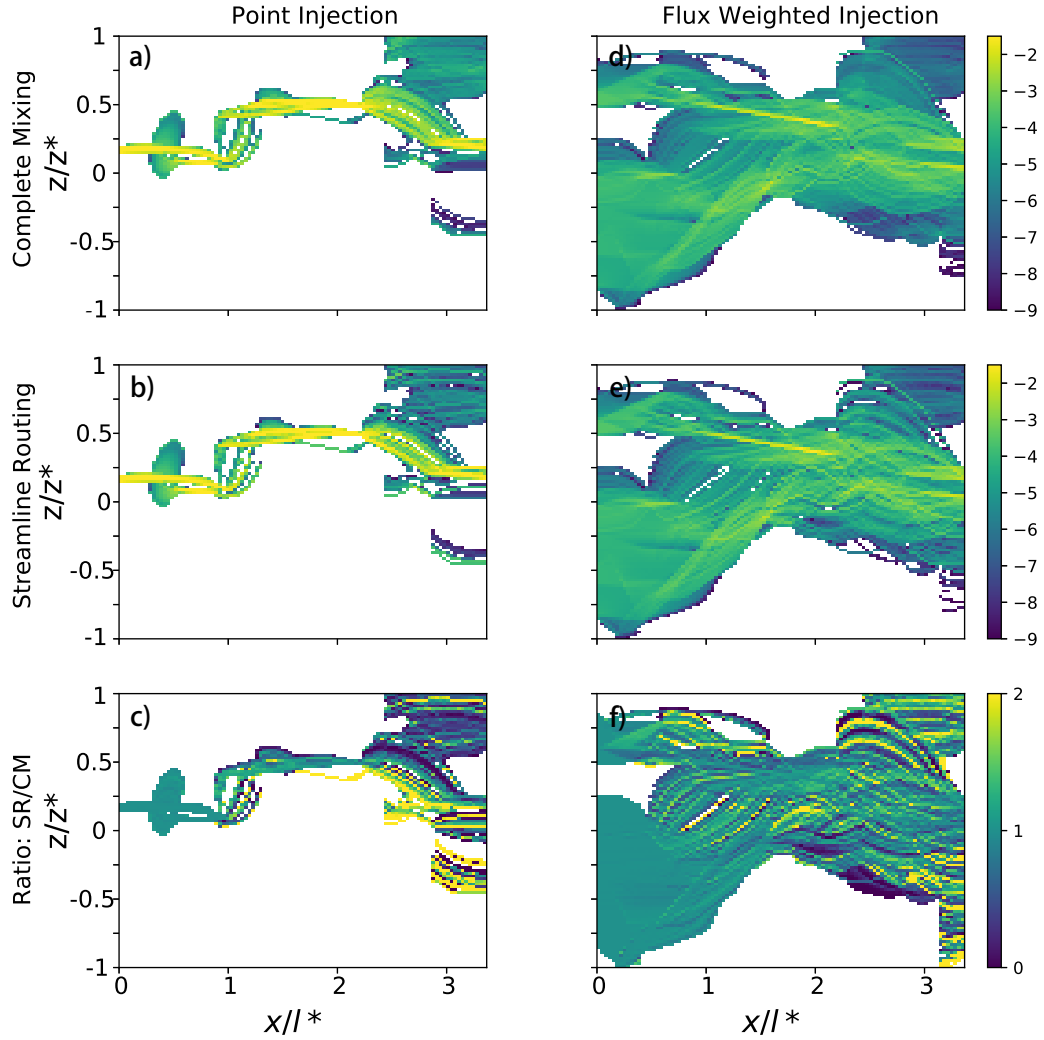


FIG. 9. The transverse breakthrough z -position distribution for one realization of a TPL network for a point (left column) and flux weighted (right column) initial injection mode. Simulations are completed for complete mixing (row 1: a,d) and streamline routing (row 2: b,e) intersection rules. Row 3 gives the ratio of streamline routing to complete mixing transverse breakthrough position concentrations. Colorbars show log probabilities (row 1,2: a,b,d,e) and the absolute ratio value (row 3: c,f). Streamline routing increases channelization of particles to secondary fractures, shown as areas of yellow in the ratio figures. The transverse direction z is normalized by half the length of domain z^* .

417 injection modes. The percent of particles on primary fractures remains similar across mixing
 418 rules and over 50% of particles at a given control plane are concentrated on less than 10% of
 419 the total fractures in the system. In the case of point injection, there are primary fractures
 420 as indicated by the brightly colored areas lying between 0 and 0.5 in z/z^* . Between 0 and 2
 421 x/l^* there is a relatively low number of fracture intersections and particles trajectories are
 422 similar. In this region the ratio of streamline routing to complete mixing TBPD is $O(1)$. At a
 423 distance greater than 2 in x , the fracture intersection density increases and complete mixing
 424 more evenly distributes particles across secondary fractures, observed as a more uniform
 425 color in TBPD distributions. In streamline routing, increased channelization to secondary
 426 fractures is observed as an increased number of streaks in the TBPD, particularly prevalent
 427 in the top and bottom right corners of the TBPD figures. These streaks also appear as
 428 yellow areas in the bottom figure that shows the ratio of the concentration for the two rules.

429 With a flux weighted initial condition, the mixing rule again causes significant differ-
 430 ences in TPBD on secondary fractures, observed as an increased number of streaks in the
 431 streamline routing simulations. However, the general evolution of particle spreading remains
 432 similar. Areas of high particle concentration (green and yellow colors) are similar for each
 433 mixing rule. There is a primary fracture (brightly colored) that extends from 1 to 2 in x
 434 and 0 to 0.5 in z that has a streamline routing TBPD to complete mixing TBPD of $O(1)$,
 435 indicating particle concentration on this fracture is approximately equal.

436 Figure 10 shows the MSD, averaged over all particles in the 10 realizations of TPL
 437 networks, for complete mixing (green) and streamline routing (orange) with a point (solid
 438 lines) and flux weighted (dashed lines) injection. There is less spatial variability in MSD for
 439 the flux weighted injection condition. As opposed to the lattice, the complicated network
 440 structure constrains the spreading of particles thereby limiting the impact of the mixing
 441 rule on MSD. The observed channelization due to streamline routing has a small impact
 442 on average particle behavior. The mean (averaged over all particles and all realizations)
 443 number of times a particle changes fractures from inlet to outlet increases approximately
 444 5% from 7.7 in complete mixing to 8.0 in streamline routing. This change percentage is less
 445 than in the lattice because the fracture intersection density is lower in the TPL networks.
 446 Consistent with the point injection on the lattice, MSD increases with increasing distance
 447 from the initial point of injection.

448 In the case of the flux-weighted injection, the mean number of times particles change

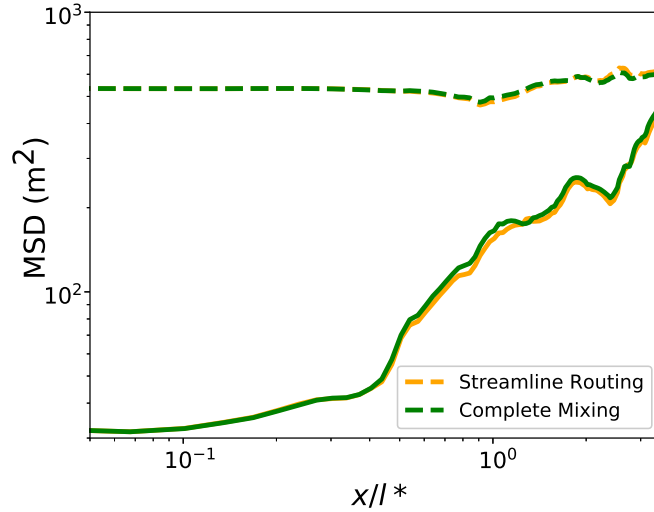


FIG. 10. The MSD is averaged over all particles in 10 realizations of stochastically generated TPL networks for complete mixing (green) and streamline routing (orange) with a point (solid lines) and flux weighted (dashed lines) injection. The MSD for the flux weighted injections has less spatial variability. The network structure drives particle spreading and so the impact of the mixing rule on MSD is negligible.

449 fractures increases 5% from 6.2 for complete mixing to 6.5 for streamline routing. The flux
 450 weighted initial condition increases the initial spread of particles compared to the point in-
 451 jection, which allows transverse breakthrough to occur across a larger portion of the domain.
 452 Hence, the flux weighted injection increases MSD at all measured control planes. As was
 453 the case for the point injection, the MSD values are nearly the same for both mixing rules.
 454 Similar to the lattice flux weighted injection simulations, MSD remains relatively constant as
 455 distance from the inlet increases, with spatial changes resulting from the network structure
 456 and not the mixing rule.

457 V. DISCUSSION

458 The results of the simulations presented in the previous section indicate that there are
 459 scenarios where the choice of mixing rule at fracture intersections can have a large impact
 460 on transport behavior and other scenarios where the impact is negligible. As noted in the
 461 introduction, this is consistent with the literature where seemingly opposite statements are

462 made with regard to how important is the mixing rule. The magnitude of the mixing rule's
463 influence is determined by how particles enter the network, the complexity of the fracture
464 network, and the heterogeneity of the velocity field.

465 **A. Injection Mode**

466 There are two major differences between the flux weighted and point injection modes
467 that cause differences in solute spreading. First, a point injection releases particles onto one
468 fracture and all particles are influenced by the same local effects near the injection point.
469 Therefore, the initial behavior is highly dependent on where the particles are released. The
470 flux weighted initial condition spreads particles across the entire inlet, thereby reducing the
471 impact of such local effects and reflecting a more broad statistical sampling of the hetero-
472 geneous system. Second, a flux weighted injection channelizes particles to high discharge
473 fractures from the start of the simulation. The flux weighted injection weights high dis-
474 charge fractures more than low discharge fractures by distributing particles proportionally
475 to fracture discharge, meaning particles channelize on primary fractures immediately. As
476 a fracture's discharge increases the probability of a particle leaving that fracture decreases.
477 Thus the mixing rule's impact decreases as more particles are distributed to high discharge
478 fractures because particles preferentially remain on these high discharge pathways. This
479 decreased impact is demonstrated by similar TPBD evolution for each mixing rule when
480 particles are flux weighted injected.

481 In a large enough network, the initial distribution of Lagrangian velocities evolves to an
482 asymptotic stationary distribution, where Lagrangian velocities becomes proportional to
483 the local velocity field, i.e. the transverse concentration distribution for the point injection
484 will converge to the flux weighted injection concentration distribution. The time needed to
485 for this to occur can be characterized with a Taylor-like timescale, $T_T = \frac{a^2}{D_T}$, where a is a
486 characteristic length and D_T is effective dispersion. In both network structures we observe
487 that the point injected MSD approaches the flux weighted MSD as distance (and time) from
488 particle release increase. Note that a and D_T are strongly affected by the network geometry
489 and so T_T changes with varying network structures. Additionally, the mixing rule influences
490 D_T ; mainly complete mixing increases D_T , and thus T_T decreases.

491 In a regularized geometry, such as the lattice, we observed complete mixing enhances

492 initial particle spreading for a point injection (Figure 4). At the length scales considered,
 493 the point injection breaks Lagrangian ergodicity, that is the Lagrangian velocity statistics
 494 sampled along a particle trajectory is not equivalent to an ensemble average across all
 495 particle velocities. Dentz et al. [52] showed that in steady heterogenous flows, a Lagrangian
 496 distribution found by spatially sampling along particle trajectories is stationary if the initial
 497 particle velocity distribution is equivalent to the Eulerian flux weighted velocity distribution.
 498 Once sufficient time has passed and the initial condition is erased, ergodicity is established
 499 and the mixing rule becomes negligible for transverse particle spreading (Figure 5). Since
 500 ergodicity is not established at pre-asymptotic times for a point injection, the mixing rule
 501 does impact spreading on the lattice. However, in networks with highly heterogeneous
 502 structures, network geometry becomes increasingly important and the impact of the injection
 503 mode decreases. For example, in the TPL networks there is a relatively small number of
 504 fracture intersections and so particle transport is constrained by the network geometry and
 505 the injection mode and mixing rule has negligible impact even at pre-asymptotic times
 506 (Figure 9).

507 B. Network Structure

508 A fracture network's geometry, specifically the fracture intersection density and fracture
 509 orientation, constrains plume spreading. As the fracture intersection density increases, par-
 510 ticles have an increased probability of changing fractures. The lattice network has a higher
 511 density of fracture intersections than the TPL networks and all intersections are continuous
 512 junctions, i.e. incoming inlets are adjacent. Therefore the mixing rule more significantly
 513 impacts particle spreading behavior. In continuous junctions, streamline routing increases
 514 the probability of changing fractures (to the adjacent) by a factor of $\frac{q_{adj}+q_{opp}}{q_{adj}}$ or $\frac{q_{adj}+q_{opp}}{q_{in}}$
 515 when $q_{in} < q_{adj}$ and $q_{in} > q_{adj}$, respectively. In the lattice network, particles regularly visit
 516 fracture intersections and streamline routing probabilistically directs more particles to adja-
 517 cent fractures, causing particle pathlines to more frequently alternate between positive and
 518 negative directions. This alternating pattern of positives and negatives cancel, focusing the
 519 particle concentration near the initial inlet transverse position (Figure 4). Hence, particle
 520 pathlines are significantly altered by the intersection mixing rule, especially when outlet
 521 discharges are similar in magnitude.

522 The 3D geometry and reduced connectivity of the TPL networks results in transport that
523 is constrained by geometrical and topological network properties. In turn, these features,
524 which are far more complex than the quasi-2D lattice, decreases the impact of the mixing
525 rule relative to the lattice. One such geometrical effect, local flow cells, develop from vari-
526 ations in fracture radii length and orientation, which manifests as elongated tails in solute
527 breakthrough [53]. Additionally, particles remain on fractures for longer distances because
528 they encounter fewer intersections, i.e., solute spreading is structurally constrained. More-
529 over, fracture aperture is positively correlated to the fracture radius in the TPL networks.
530 By nature of the truncated power law distributions a small percentage of fractures will
531 therefore have substantially larger permeability and dominate transport due to geometric,
532 topological, and hydrological preference. In combination, these attributes dominant local
533 flow behavior and decreases the impact of the mixing rule.

534 Furthermore, streamline routing increases the probability of transferring particles to the
535 adjacent fracture in a continuous intersection by a factor of $\frac{q_{adj}+q_{opp}}{q_{in}}$ for $q_{in} > q_{adj}$, which is
536 typical in the case of a particle traveling on a preferential flow path. For a particle traveling
537 on such a pathway (which is the majority) in the TPL network, $q_{in} \approx q_{out}$ as they lie on the
538 same fracture; $q_{in} \gg q_{adj}$ is expected due to the fracture length distribution. This suggests
539 that the probability of a particle changing fractures remains nearly identical ($\frac{q_{adj}+q_{opp}}{q_{in}} \approx 1$)
540 between streamline routing and complete mixing, and the choice of mixing rule is negligible
541 in networks with strong preferential flow pathways, such as the TPL networks considered in
542 this study.

543 C. Velocity Field Heterogeneity

544 Closely coupled with the network structure is the velocity field heterogeneity. In fact,
545 Margolin et al. [54] found that increasing the network sparseness has the same effect as
546 increasing the velocity field heterogeneity. As the difference between incoming discharge
547 magnitudes increases, the probability of being routed to the higher magnitude outlet also
548 increases and the impact of the mixing rule decreases. On the lattice, velocity field hetero-
549 geneity increases as the variance of the fracture aperture distribution increases. Increasing
550 velocity heterogeneity leads to the development of preferential flow paths in large aperture
551 regions [55], which cause greater channelization of particles and form a subnetwork of frac-

552 tures that dominate transport. The mean number of times a particle changes fractures
553 decreases with increasing velocity heterogeneity because the probability of transferring from
554 primary fractures decreases. Additionally, the difference in the number of fracture changes
555 between mixing rules also decreases as the velocity field heterogeneity increases. Hence, par-
556 ticle pathlines become more similar and the mixing rule’s impact decreases as the velocity
557 heterogeneity increases, which is consistent with the conclusions of Kang et al. [10].

558 In the TPL networks, discharge through a fracture is directly related to the fracture radii,
559 hence the distribution of fracture sizes naturally forms a highly heterogeneous velocity field.
560 The evolution of transverse spreading for both mixing rules looks very similar through TPL
561 networks because the large radii fractures channelize particles and the network geometry
562 drives overall spreading trends. In addition to the velocity field heterogeneity, other factors
563 control transport and reduce the impact of the mixing rule, e.g. network connectivity and
564 geometry [56]. In the context of conservative transport, the higher heterogeneity of the
565 TPL network makes the impact of the mixing rule negligible on spreading metrics, a finding
566 consistent with Park et. al. [19] who studied conservative transport through 2D DFNs with
567 power law radii distributions.

568 **D. Implications for Reactive Transport**

569 The results of this study suggest that the mixing rule has a small impact on common
570 conservative transport metrics, i.e. breakthrough curves; mean square displacement; and the
571 general distribution of TBPD, in complicated geologic media where the network structure
572 and velocity field are often highly heterogeneous. While these metrics quantify transport
573 behavior at the network scale there are smaller-scale physical and chemical variations in
574 geologic media that are important in the context of reactive transport [57]. In this study we
575 observe that the mixing rule significantly impacts channelization of particles at the fracture
576 scale. Such channelization is important because it drives solute together, enhancing the
577 mixing rate and increasing the probability that two species react [24]. Zho et al. [18] showed
578 that the fracture surface roughness increases particle channelization through an intersection,
579 thereby increasing solute mixing at the fracture intersection scale. Similarly, we investigate
580 how channelization due to the intersection mixing rule influence solute mixing, and thus
581 reactions, at the fracture scale.

582 Consider a system with two reactive species A and B , who undergo the irreversible
583 chemical reaction $A + B \rightarrow C$, such as precipitation of a mineral and two ions [58–61]. The
584 nature of such reaction requires the difference in concentrations of species to be conserved.
585 Denote u as the conserved quantity, where $u = c_A - c_B$ and c_i is the concentration of species
586 i [58]. Consequently, the amount of C that can be precipitated is dependent on the less
587 abundant species between A and B . In geochemical systems described by instantaneous
588 equilibrium reactions, De Simoni et al. [58] showed the reaction rate between A and B
589 is a product of a flow driven mixing term $\nabla^T u \nabla u$ and a stoichiometric term. Hence, the
590 mixing rate is directly related to the rate of reaction. The mixing rate is independent of
591 the chemical effects. Since u and particles in DFNWORKS are both conserved quantities
592 and have the same governing equations, we can measure u and therefore the mixing rate.
593 Similar to the TBPD measured in Figure 9, we also measure the joint $y - z$ breakthrough
594 position distribution at each control plane, i.e. we discretize each control plane into a 2D
595 grid and measure breakthrough concentration in each cell. This enables construction of
596 the 3D position breakthrough field. The position breakthrough field provides the entire
597 u -concentration field that arises after large time in a steady flow, in which u particles are
598 continuously injected. The mixing rate is calculated from this u -concentration field.

599 The ratio of computed mixing rates using streamline routing and complete mixing is
600 plotted throughout the three dimensional domain (Figure 11) for one network realization
601 with a point injection (a) and flux weighted injection (b). The injection plane is on the front
602 right face and the primary flow direction is directed to the back left face in both sub figures.
603 The ratio of mixing rates at areas near the inlet where particles have yet to encounter a
604 fracture intersection is 1. After particles pass through fracture intersections, the mixing
605 rule distributes particles differently causing significant local effects in the mixing rates, e.g.
606 notice the yellow colored streak intersecting the outlet plane where the local mixing rate
607 differs by two orders of magnitudes.

608 Figure 12 shows the mean normalized mixing rate at each control plane averaged over all
609 realizations for a point injection (a) and flux weighted injection (b) in the TPL networks.
610 For each realization, the mixing rate is normalized by the maximum mixing rate observed in
611 the streamline routing case. On average, streamline routing elevates the mean mixing rate
612 for both modes of injection. The mixing rate is similar across mixing rules when $x^*/l < 1$,
613 which corresponds to a distance equal to the radii of the largest fracture in the network.

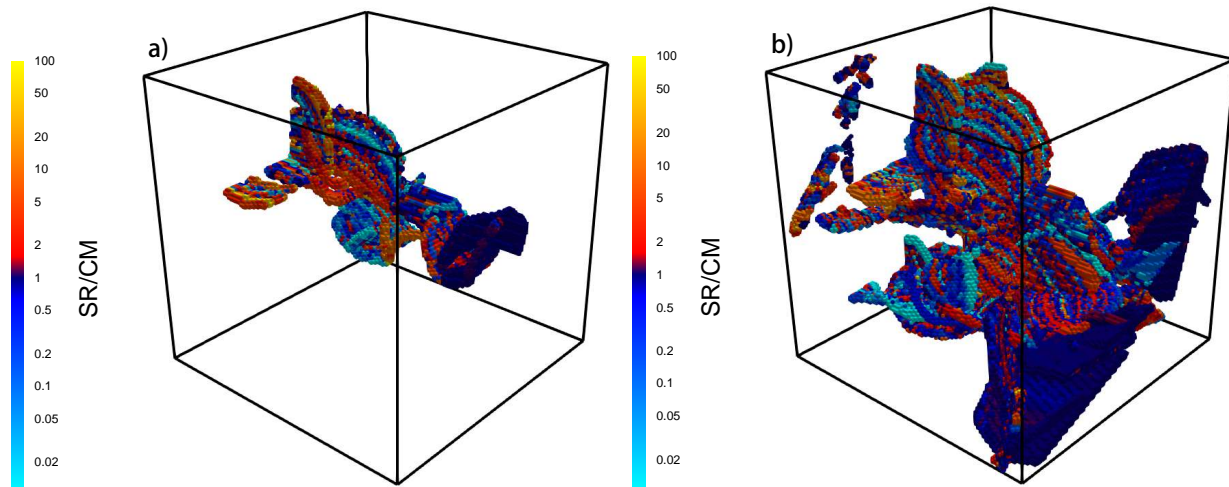


FIG. 11. The ratio streamline routing to complete mixing local mixing ratios is shown for one TPL network realization for a point (a) and flux weighted (b) initial injection. The front right face is the plane of injection and the back left face is the domain outlet. Color bars plot the absolute ratio value. Near the inlet plane, the ratio between mixing rules is 1 because transport has yet to encounter fracture intersections. Near the outlet plane, we observe streaks where local mixing rates differ by a factor of 100. Differences in mixing rate occur from differences in channelization of particles due to the mixing rule.

614 After traveling this distance, the mixing rate is noticeably greater when streamline routing
 615 is used in the domain.

616 The transverse breakthrough position distributions in the TPL networks display increased
 617 channelization of particles on secondary fractures for a streamline routing mixing rule, cf.
 618 Fig. 9. These regions of increased channelization are therefore also areas of increased mixing.
 619 Hence, it is expected that streamline routing increases the average mixing rate at each
 620 control plane. Figure 12 shows that streamline routing increases the mean mixing rate at
 621 a distance of approximately equal to the length of the largest fracture radii in the system
 622 l^* . Near the particle source, the mixing rule has a smaller impact on channelization because
 623 particles have encountered less fracture intersections. At distances exceeding l^* a particle
 624 must have encountered at least one fracture intersection and so the mixing rule becomes more
 625 important, as fracture intersections enable particles to be channelized to other fractures.

626 At the fracture scale the local mixing rate can differ by a factor of 100 or greater between

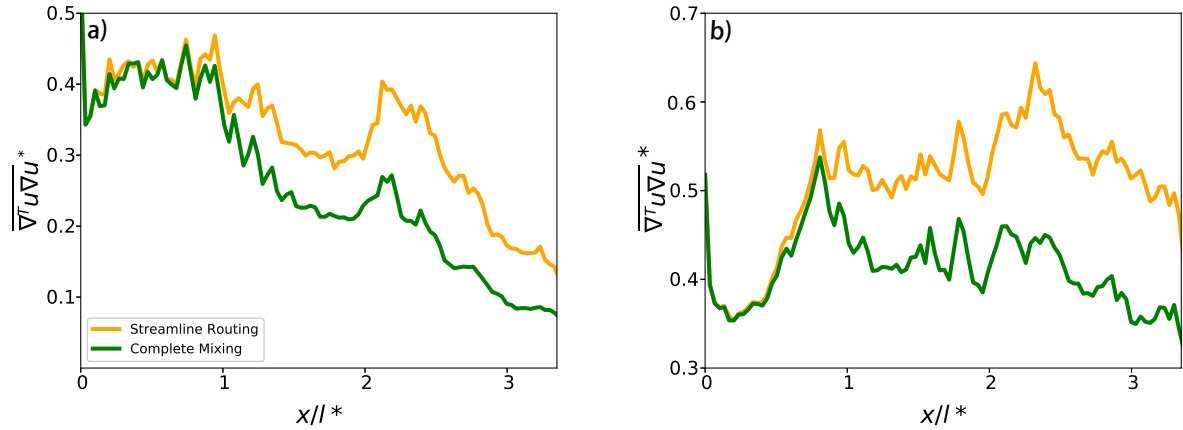


FIG. 12. The mean mixing rate averaged over 10 TPL realizations at each control plane is compared for complete mixing (green) and streamline routing (orange) with a point injection (a) and flux weighted (b) initial injection. In each realization, the mixing rate is normalized by maximum mixing rate observed for streamline routing. Streamline routing increases the mean mixing rate. At distances greater than l^* from the particle source the difference between mixing rules is greater because particles have encountered at least one fracture intersection.

627 the different mixing rules. Such large variation occurs on smaller fractures, which are more
 628 sensitive to the mixing rule. Large fractures are less sensitive to the mixing rule because
 629 they carry more particles and the probability of switching from them is lower, meaning the
 630 concentration gradient is more stable. In systems where solute and the rock boundary react
 631 to dissolve and precipitate minerals, a large difference in mixing rate may lead to significant
 632 differences in the temporal evolution of transport. Hence implementing the most physically
 633 appropriate mixing rule is necessary for developing reliable predictive DFN modeling of
 634 reactive transport.

635 Cvetkovic et al. [5] simulated sorbing tracers through a 3D DFN. Reactive transport
 636 was quantified with a hydrodynamic retention variable β , which is a normalized surface
 637 area for diffusion transfer into the rock boundary [62]. They found that streamline routing
 638 has a small impact on β compared with complete mixing, but streamline routing does
 639 slightly shift β towards higher values. The increased β suggests streamline routing is more
 640 reactive. These results are consistent with our observations of increased channelization
 641 to secondary fractures under streamline routing, as β increases as aperture size decreases
 642 and secondary fractures typically have smaller apertures than primary fractures. β is an

643 averaged parameter over particle trajectories and so the significant local effects observed
644 in this studied are not apparent by a slightly increased value. The results of our study
645 suggest that the slight increase in β observed by Cvetkovic et. al [62]. could be the result
646 of increased channelization of particles to secondary fractures with streamline routing.

647 VI. REMARKS

648 We presented a study characterizing the impact of particle behavior at fracture intersec-
649 tions in three-dimensional DFNs on upscaled transport behavior. Mass transfer at fracture
650 intersections in DFN models is represented with two subgrid processes, complete mixing
651 and streamline routing, which are the end member cases of the Péclet number, i.e. particle
652 motion through a fracture intersection is governed only by diffusion or advection, respec-
653 tively. The simulations presented in the previous section indicate that there are scenarios
654 where the choice of mixing rule at fracture intersections have a large impact on transport
655 behavior and other scenarios where the impact is negligible. The magnitude of impact of
656 the mixing rule is determined by the particle initial injection mode, the fracture network
657 structure, and the heterogeneity of the velocity field. The mixing rule's impact increases
658 with a point injection because local effects associated with the fracture of injection control
659 initial particle transport. As the network geometry and velocity field heterogeneity increase,
660 particle channelization to high discharge fractures increase and the impact of the mixing rule
661 on conservative transport at the network scale decreases. In all cases, however, streamline
662 routing increases channelization of mass to secondary fractures, resulting in an increased
663 average mixing rate and local mixing rates that can differ by two orders of magnitude.
664 Therefore, the choice of mixing rule at fracture intersections will influence reactive trans-
665 port simulations within DFN models. We consider the two end members for intersection
666 mixing rules and our simulations enforce that every intersection prescribes to the same rule.
667 In real geologic media, both advection and diffusion affect mass transfer and a distribution
668 of local fracture intersection Pe exists. Quantifying the impact of these processes warrants
669 future investigation.

670 **ACKNOWLEDGEMENTS**

671 TS is thankful for support from the Center For Nonlinear Studies at Los Alamos National
672 Laboratory. JDH is thankful for support from the LANL-LDRD grant # 20180621ECR. TS,
673 JDH, and GS are thankful for support from the LANL-LDRD grant # 20170103DR. DB and
674 TS expresses thanks for financial support via NSF Grants EAR-1351625, EAR-1446236 and
675 CBET-1803989. NM is thankful for support from the Used Fuel Disposition Campaign of
676 the United States Department of Energy. This work was funded by the Department of En-
677 ergy at Los Alamos National Laboratory under contract DE-AC52-06NA25396 through the
678 Laboratory-Directed Research and Development Program. We also are grateful to Shriram
679 Srinivasan for his help generating networks. LA-UR-18-29382

680 **REFERENCES**

-
- 681 [1] E. Bonnet, O. Bour, N. E. Odling, P. Davy, I. Main, P. Cowie, and B. Berkowitz, *Rev.*
682 *Geophys.* **39**, 347 (2001).
- 683 [2] S. Pacala and R. Socolow, *Science* **305**, 968 (2004).
- 684 [3] E. Barbier, *Renew. Sust. Energ. Rev.* **6**, 3 (2002).
- 685 [4] J. Hyman, J. Jiménez-Martínez, H. Viswanathan, J. Carey, M. Porter, E. Rougier, S. Karra,
686 Q. Kang, L. Frash, L. Chen, *et al.*, *Phil. Trans. R. Soc. A* **374**, 20150426 (2016).
- 687 [5] V. Cvetkovic, S. Painter, N. Outters, and J. Selroos, *Water Resour. Res.* **40** (2004).
- 688 [6] J. Hyman and J. Jiménez-Martínez, *Water Resour. Res.* **54**, 3243 (2018).
- 689 [7] J.-R. de Dreuzy, Y. Méheust, and G. Pichot, *J. Geophys. Res.-Sol. Ea.* **117** (2012).
- 690 [8] N. Makedonska, J. D. Hyman, S. Karra, S. L. Painter, C. W. Gable, and H. S. Viswanathan,
691 *Adv. Water Resour.* **94**, 486 (2016).
- 692 [9] J. Johnson, S. Brown, and H. Stockman, *J. Geophys. Res.-Sol. Ea.* **111** (2006).
- 693 [10] P. K. Kang, M. Dentz, T. Le Borgne, and R. Juanes, *Phys. Rev. E* **92**, 022148 (2015).
- 694 [11] R. J. Krizek, G. M. Karadi, and E. Socias, paper presented at Symposium on Percolation
695 Through Fissured Rock, *Int. Soc. of Rock Mech.*, Stuttgart, Germany (1972).
- 696 [12] C. R. Wilson and P. Witherspoon, *Water Resour. Res.* **12**, 102 (1976).

- 697 [13] L. Hull and K. Koslow, *Water Resour. Res.* **22**, 1731 (1986).
- 698 [14] J. W. Robinson and J. E. Gale, *Groundwater* **28**, 25 (1990),
699 <https://onlinelibrary.wiley.com/doi/pdf/10.1111/j.1745-6584.1990.tb02226.x>.
- 700 [15] B. Berkowitz, C. Naumann, and L. Smith, *Water Resour. Res.* **30**, 1765 (1994).
- 701 [16] H. W. Stockman, C. Li, and J. L. Wilson, *Geophys. Res. Lett.* **24**, 1515 (1997).
- 702 [17] V. Mourzenko, F. Yousefian, B. Kolbah, J.-F. Thovert, and P. Adler, *Water Resour. Res.* **38**
703 (2002).
- 704 [18] L. Zou, L. Jing, and V. Cvetkovic, *Adv. Water Resour.* **107**, 1 (2017).
- 705 [19] Y. J. Park, J. de Dreuzy, K. K. Lee, and B. Berkowitz, *Water Resour. Res.* **37**, 2493 (2001).
- 706 [20] J. Küpper, F. Schwartz, and P. Steffler, *J. Contam. Hydrol.* **18**, 33 (1995).
- 707 [21] Y. J. Park, K. K. Lee, and B. Berkowitz, *Water Resour. Res.* **37**, 909 (2001).
- 708 [22] J. D. Hyman, S. Karra, N. Makedonska, C. W. Gable, S. L. Painter, and H. S. Viswanathan,
709 *Comput. Geosci.* **84**, 10 (2015).
- 710 [23] T. Aquino and D. Bolster, *Transport in Porous Media* **119**, 391 (2017).
- 711 [24] E. E. Wright, D. H. Richter, and D. Bolster, *Phys. Rev. Fluids* **2**, 114501 (2017).
- 712 [25] S. P. Neuman, *Hydrogeology Journal* **13**, 124 (2005).
- 713 [26] P. Lichtner, G. Hammond, C. Lu, S. Karra, G. Bisht, B. Andre, R. Mills, and J. Kumar,
714 *PFLOTRAN User Manual: A Massively Parallel Reactive Flow and Transport Model for*
715 *Describing Surface and Subsurface Processes*, Tech. Rep. ((Report No.: LA-UR-15-20403) Los
716 Alamos National Laboratory, 2015).
- 717 [27] M.-C. Cacas, E. Ledoux, G. d. Marsily, B. Tillie, A. Barbreau, E. Durand, B. Feuga, and
718 P. Peaudecerf, *Water Resour. Res.* **26**, 479 (1990).
- 719 [28] J.-R. de Dreuzy, C. Darcel, P. Davy, and O. Bour, *Water Resour. Res.* **40** (2004).
- 720 [29] I. Bogdanov, V. Mourzenko, J.-F. Thovert, and P. Adler, *Phys. Rev. E* **76**, 036309 (2007).
- 721 [30] J. D. Hyman, S. L. Painter, H. Viswanathan, N. Makedonska, and S. Karra, *Water Resour.*
722 *Res.* **51**, 7289 (2015).
- 723 [31] J. D. Hyman, G. Aldrich, H. Viswanathan, N. Makedonska, and S. Karra, *Water Resour.*
724 *Res.* **52**, 6472 (2016).
- 725 [32] S. Karra, N. Makedonska, H. Viswanathan, S. Painter, and J. Hyman, *Water Resour. Res.*
726 **51**, 8646 (2015).

- 727 [33] J. D. Hyman, C. W. Gable, S. L. Painter, and N. Makedonska, *SIAM J. Sci. Comput.* **36**,
728 A1871 (2014).
- 729 [34] LaGriT, “Los Alamos Grid Toolbox, (LaGriT) Los Alamos National Laboratory,”
730 <http://lagrit.lanl.gov> (2013).
- 731 [35] N. Makedonska, S. L. Painter, Q. M. Bui, C. W. Gable, and S. Karra, *Computat. Geosci.* **19**,
732 1123 (2015).
- 733 [36] S. Painter, C. Gable, and S. Kelkar, *Computat. Geosci.* **16**, 1125 (2012).
- 734 [37] A. Kreft and A. Zuber, *Chemical Engineering Science* **33**, 1471 (1978).
- 735 [38] A. Frampton and V. Cvetkovic, *Water Resour. Res.* **47** (2011).
- 736 [39] J. Philip, *Water Resour. Res.* **24**, 239 (1988).
- 737 [40] X. Sanchez-Vila, A. Guadagnini, and J. Carrera, *Rev. Geophys.* **44** (2006).
- 738 [41] J.-R. de Dreuzy, P. Davy, and O. Bour, *Water Resour. Res.* **37**, 2079 (2001).
- 739 [42] J. Long and D. M. Billaux, *Water Resour. Res.* **23**, 1201 (1987).
- 740 [43] O. Bour and P. Davy, *Water Resources Research* **33**, 1567 (1997).
- 741 [44] P. Davy, *Journal of Geophysical Research: Solid Earth* **98**, 12141 (1993).
- 742 [45] N. E. Odling, *Journal of Structural Geology* **19**, 1257 (1997).
- 743 [46] G. Ouillon, C. Castaing, and D. Sornette, *J. Geophys. Res.-Sol. Ea.* **101**, 5477 (1996).
- 744 [47] J.-R. de Dreuzy, P. Davy, and O. Bour, *Water Resour. Res.* **38** (2002).
- 745 [48] A. Frampton and V. Cvetkovic, *Water Resour. Res.* **46** (2010).
- 746 [49] S. Joyce, L. Hartley, D. Applegate, J. Hoek, and P. Jackson, *Hydrogeol. J.* **22**, 1233 (2014).
- 747 [50] T. P. Wellman, A. M. Shapiro, and M. C. Hill, *Water Resour. Res.* **45** (2009).
- 748 [51] J. De Dreuzy, P. Davy, and O. Bour, *Phys. Rev. E* **62**, 5948 (2000).
- 749 [52] M. Dentz, P. K. Kang, A. Comolli, T. Le Borgne, and D. R. Lester, *Phys. Rev. Fluids* **1**,
750 074004 (2016).
- 751 [53] Y. Park, K. Lee, G. Kosakowski, and B. Berkowitz,
752 *Water Resour. Res.* **39** (2003), 10.1029/2002WR001801,
753 <https://agupubs.onlinelibrary.wiley.com/doi/pdf/10.1029/2002WR001801>.
- 754 [54] G. Margolin, B. Berkowitz, and H. Scher, *Water Resources Research* **34**, 2103 (1998).
- 755 [55] S. Brown, A. Caprihan, and R. Hardy, *Journal of Geophysical Research: Solid Earth* **103**,
756 5125 (1998).

- 757 [56] P. M. Adler and J.-F. Thovert, *Fractures and fracture networks*, Vol. 15 (Springer Science &
758 Business Media, 1999).
- 759 [57] M. Dentz, T. Le Borgne, A. Englert, and B. Bijeljic, *Journal of contaminant hydrology* **120**,
760 1 (2011).
- 761 [58] M. D. Simoni, J. Carrera, X. Sanchez-Vila, and A. Guadagnini, *Water Resour. Res.* **41** (2005).
- 762 [59] M. De Simoni, X. Sanchez-Vila, J. Carrera, and M. Saaltink, *Water Resour. Res.* **43** (2007).
- 763 [60] L. D. Donado, X. Sanchez-Vila, M. Dentz, J. Carrera, and D. Bolster, *Water Resour. Res.*
764 **45**, W11402 (2009).
- 765 [61] X. Fu, L. Cueto-Felgueroso, D. Bolster, and R. Juanes, *J. Fluid Mech.* **764**, 296 (2015).
- 766 [62] V. Cvetkovic, J. Selroos, and H. Cheng, *J. Fluid Mech.* **378**, 335 (1999).